Supporting Information

Chu et al. 10.1073/pnas.1702226114

SI Materials and Methods

Contour Detection. To detect a nuclear contour, we used a custom-written MatLab (The MathWorks) code. The contours were detected by watershed method. Since the images of CGS (H2B-GFP) and NE (LMNA-GFP) have two local minima, inside and outside the nucleus, for each image, we need to create a mask to implement watershed on these two regions. To create a mask, a preliminary edge was required and was determined via finding the local maximum of the gradient of the image. The preliminary edge was dilated to get the mask for outside the nucleus and was eroded to get the mask for inside the nucleus. These two masks were added to get the final mask for watershed. To obtain the contour, we needed to take the gradient of the original image, impose the mask on it, and apply watershed on the masked gradient. The contour was converted to binary image for the following analysis. The precision of this detection was estimated to be 20 nm.

Analysis of Contour Shape Fluctuations. The following analysis was described in detail in ref. 7. After having determined the x_i and y_i coordinates of the contour in every frame (i.e., time point t) as described in *Contour Detection*, the center of mass of the contour was determined according to

$$S_x = \frac{1}{K}\sum_{i=1}^{K} x_i, \quad S_y = \frac{1}{K}\sum_{i=1}^{K} y_i,$$

where K is the number of pixels in the contour. Further, we use the center of mass as an origin to describe the contour r by polar coordinates $r(\phi, t)$. We divided the contour line equally into 2^9 segments and calculated the average $r(\phi, t)$ lying within each segment, thus obtaining 512 equidistant points. The noise was smoothed out by averaging over the values of $r(\phi, t)$ lying within segments of $2\pi/128$ to get a new set of 512 points. To provide a measure of the shape fluctuations of the contour, we calculated u, which is the deviation of the instantaneous contour $r(\phi, t)$ from the average contour $r_0(\phi)$, by $u(\phi, t) = r(\phi, t) - r_0(\phi)$ at different time points t.

Further, we performed the Fourier transformation of the $u(\phi, t)$ using a Fast Fourier Transform procedure at every time t following $u_q(t) = 1/2\pi\int_0^{2\pi} u(\phi, t)e^{-iq\phi}\, d\phi$. The Fourier transformation yields complex Fourier coefficients, $c_q = a_q + ib_q$, where q runs from -255 to $+255$. Since the excitation modes are statistically independent, the time average of the contour is determined by averaging over the Fourier coefficients for M contours, $\overline{a}_{n,q} = 1/M\sum_{i=1}^{M} a_{i,q}$, $\overline{b}_{n,q} = 1/M\sum_{i=1}^{M} b_{i,q}$. Thus, a mean square amplitude of mode q is given by

$$\langle u_q(t)^2\rangle = \frac{1}{M}\sum_{1}^{M}[(a_{i,q} - \overline{a}_{n,q})^2 + (b_{i,q} - \overline{b}_{n,q})^2].$$

The PSD was calculated by $PSD(q) = c_q c_q^* L_c/512^2$, where c_q is the Fourier coefficient at each q, and L_c is the contour length of the nucleus.

To test our analysis code, we computed $\langle u_q(t)^2\rangle$ for a vesicle (Fig. S8), which was analyzed and data provided in ref. 41, and we calculated the bending rigidity κ of the vesicle to be about 7 $k_B T$, where k_B is the Boltzmann constant and T is the temperature. This is in agreement with previous calculations, which obtain κ from 5 $k_B T$ to 30 $k_B T$ (41, 42).

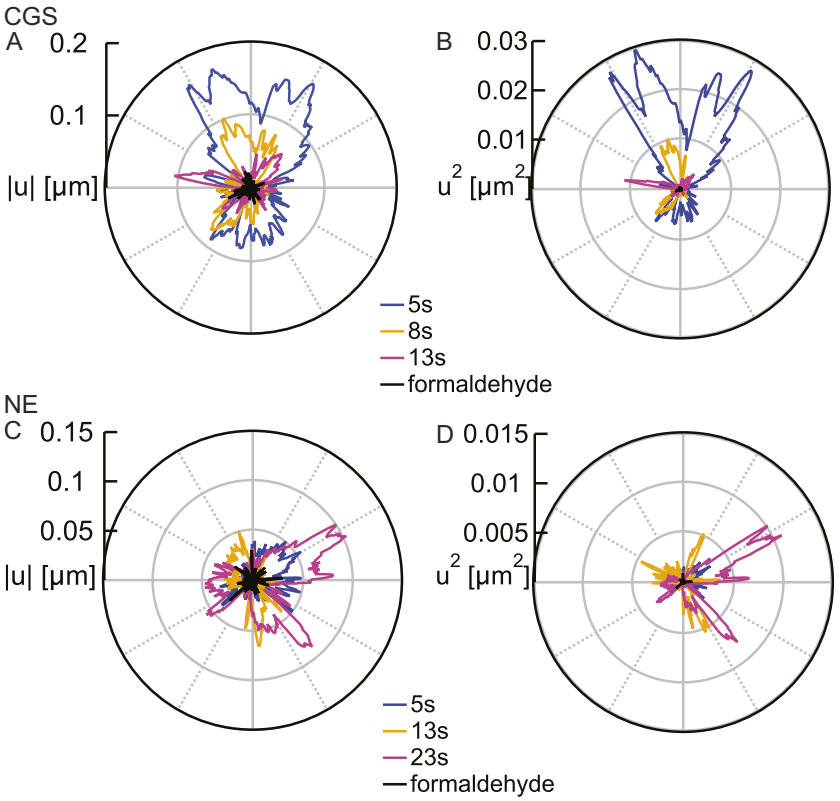

Fig. S1. In vivo measurements of the shape fluctuations of the CGS and NE. (*A*) Fluctuations u calculated for the contours of CGS from Fig. 1*B* at t = 5, 8, and 13 s. (*B*) Fluctuations u^2 calculated for the contours of CGS from Fig. 1*B* at t = 5, 8, and 13 s. (*C*) Fluctuations u calculated for the NE contours from Fig. 1*E* at t = 5, 13, and 23 s. (*D*) Fluctuations u^2 calculated for the NE contours from Fig. 1*E* at t = 5, 13, and 23 s. In addition, in *A*–*D*, we plot u and u^2 for samples fixed with formaldehyde (black), demonstrating that our measurements are well above the noise floor.

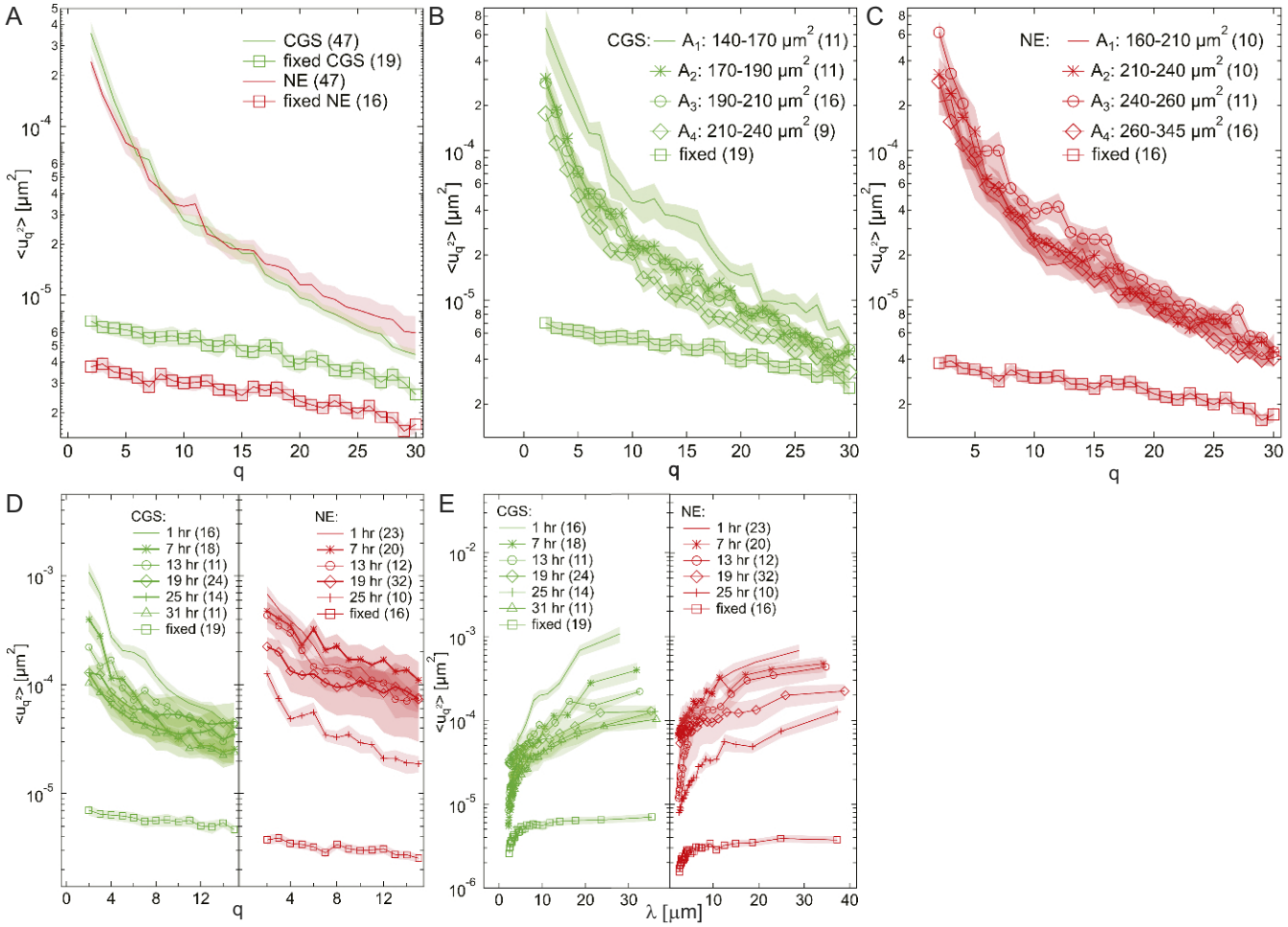

Fig. S2. Shape fluctuations of CGS and NE are cell cycle-dependent. (*A*) Wavenumber-dependent fluctuations $\langle u_q^2 \rangle$ with error bars (SE) calculated for CGS (H2B-GFP, green solid line, $n = 47$) and NE (LMNA-GFP, red solid line, $n = 47$). (*B*) The $\langle u_q^2 \rangle$ of CGS calculated with error bars (SE) for four groups determined based on their measured nuclear area *A*. (*C*) The $\langle u_q^2 \rangle$ of NE calculated with error bars (SE) for four groups determined based on their measured nuclear area *A*. (*D*) Wavenumber-dependent fluctuations $\langle u_q^2 \rangle$ with error bars (SE) of CGS (green) and NE (red) measured at different times during the cell cycle; $\langle u_q^2 \rangle$ for both CGS and NE exhibits a monotonous decrease with increasing time during the cell cycle. (*E*) Wavenumber-dependent fluctuations $\langle u_q^2 \rangle$ as a function of wavelength λ with error bars (SE) of CGS (green) and NE (red) measured at different times during the cell cycle.

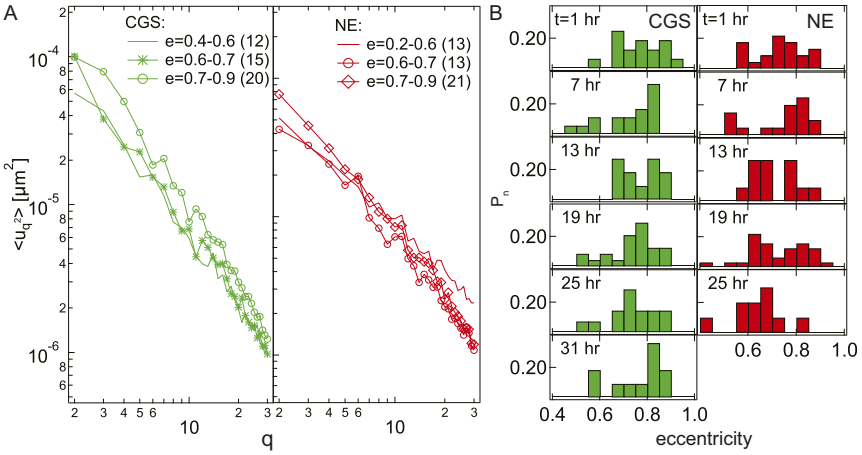

Fig. S3. Influence of average nuclear shape on the nuclear shape fluctuations. (*A*) Wavenumber-dependent nuclear fluctuations $\langle u_q^2 \rangle$ for nuclei of different eccentricity *e* for both CGS and NE. (*B*) Histograms of nuclear eccentricity *e* for CGS (green) and NE (red) measured at $t = 1$, 7, 13, 19, 25, and 31 h after the metaphase. We find no correlation between the overall nuclear shape (described by eccentricity) and $\langle u_q^2 \rangle$.

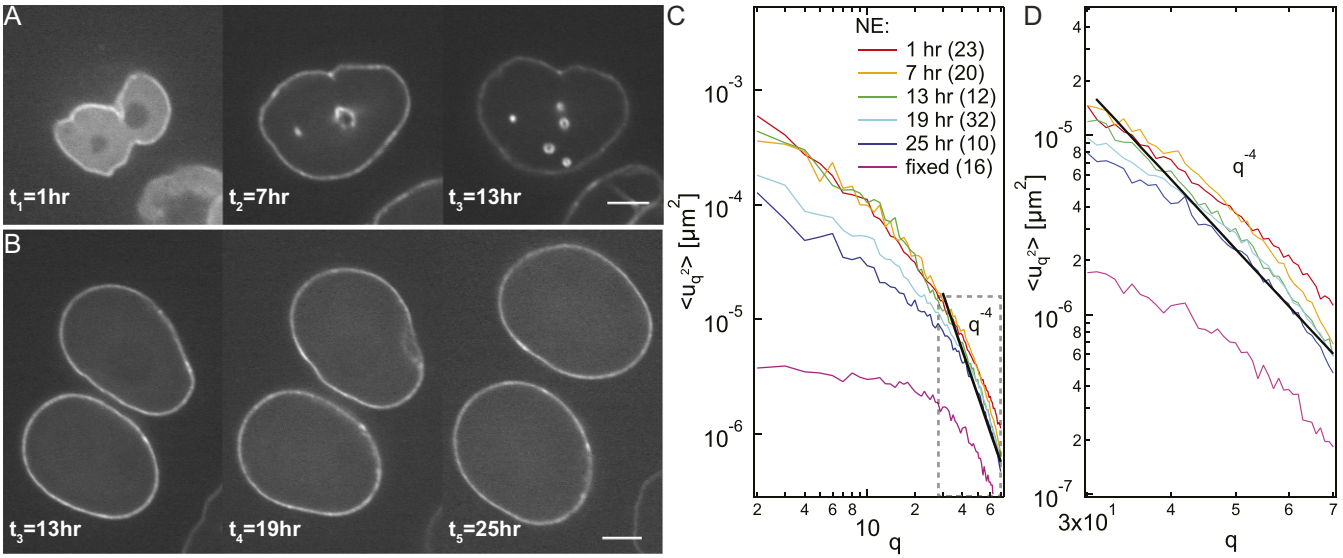

Fig. S4. Nuclear size increases with the cell cycle. (*A*) Micrographs of the same nucleus expressing LMNA-GFP taken at three different times during the cell cycle: t = 1, 7, and 13 h (where t = 0 h corresponds to the metaphase), showing a monotonous increase in the nuclear size with progressing cell cycle. (*B*) Micrographs of two cell nuclei expressing LMNA-GFP taken at three different times during cell cycle: t = 13, 19, and 25 h. (*C*) Wavenumber-dependent fluctuations $\langle u_q^2 \rangle$ of NE measured at different times during the cell cycle: t = 1, 7, 13, 19, and 25 h. A black solid line, $\sim q^{-4}$, indicates that $\langle u_q^2 \rangle$ follows this type of behavior at large q values. (*D*) Inset from *C* shows that the part of $\langle u_q^2 \rangle$ spectra that follows the $\sim q^{-4}$ behavior decreases with time, suggesting stiffening of the NE. (Scale bar, 5 μm.)

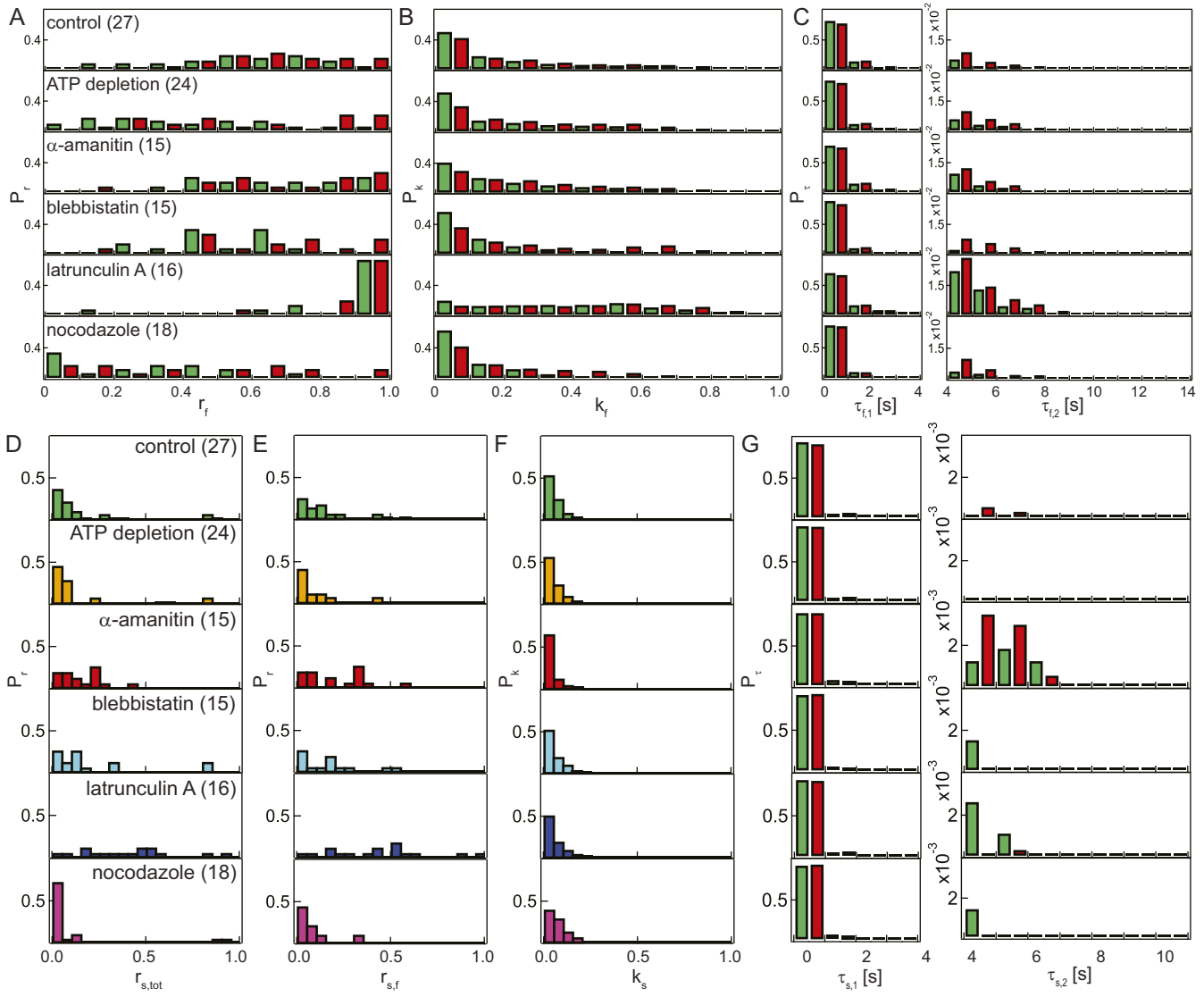

Fig. S5. Analysis of fluctuation sites upon different perturbations. (*A*) Histogram of ratio of fluctuation sites r_f for each condition. Ratio of fluctuation sites was determined by counting the sites with fluctuation ($u^2 > 0$) along the nuclear contour and normalized by its length. Green bars represent the fluctuations for CGS, where $u^2_{cgs} > 0$, and red bars represent the fluctuations for NE, where $u^2_{ne} > 0$. (*B*) Histograms of fluctuation rate k_f at each condition. The rate of a fluctuation site was calculated by counting the time points with fluctuations $u^2 > 0$ at that fluctuation site and normalized by the length of measurement (20 s). (*C*) Histogram of fluctuation duration τ_f for every condition; $\tau_{f,1}$ shows the region of short duration, and $\tau_{f,2}$ shows the region of long duration. (*D*) Histogram of ratio of separation sites $r_{s,tot}$ for each condition. Ratio of separation sites was determined by counting the sites with separation $(u_{cgs} - u_{ne})^2 \neq 0$ along the nuclear contour and normalized by its length. (*E*) Histogram of the fraction of separation sites $r_{s,f}$ distribution calculated by normalizing data from *D* by the average value of r_f obtained from *A* for each condition. (*F*) Histogram of separation rate k_s at each condition. The rate of a separation site was calculated by counting the time points with separation at that separation site and normalized by the length of measurement (20 s). (*G*) Histogram of separation duration τ_s for every condition; $\tau_{s,1}$ shows the region of short duration, and $\tau_{s,2}$ shows the region of long duration. Green bars represent $\tau_{s,2,cgs}$ for $(u^2_{ne} - u^2_{cgs}) < 0$, and red bars represent the $\tau_{s,2,ne}$ for $(u^2_{ne} - u^2_{cgs}) > 0$.

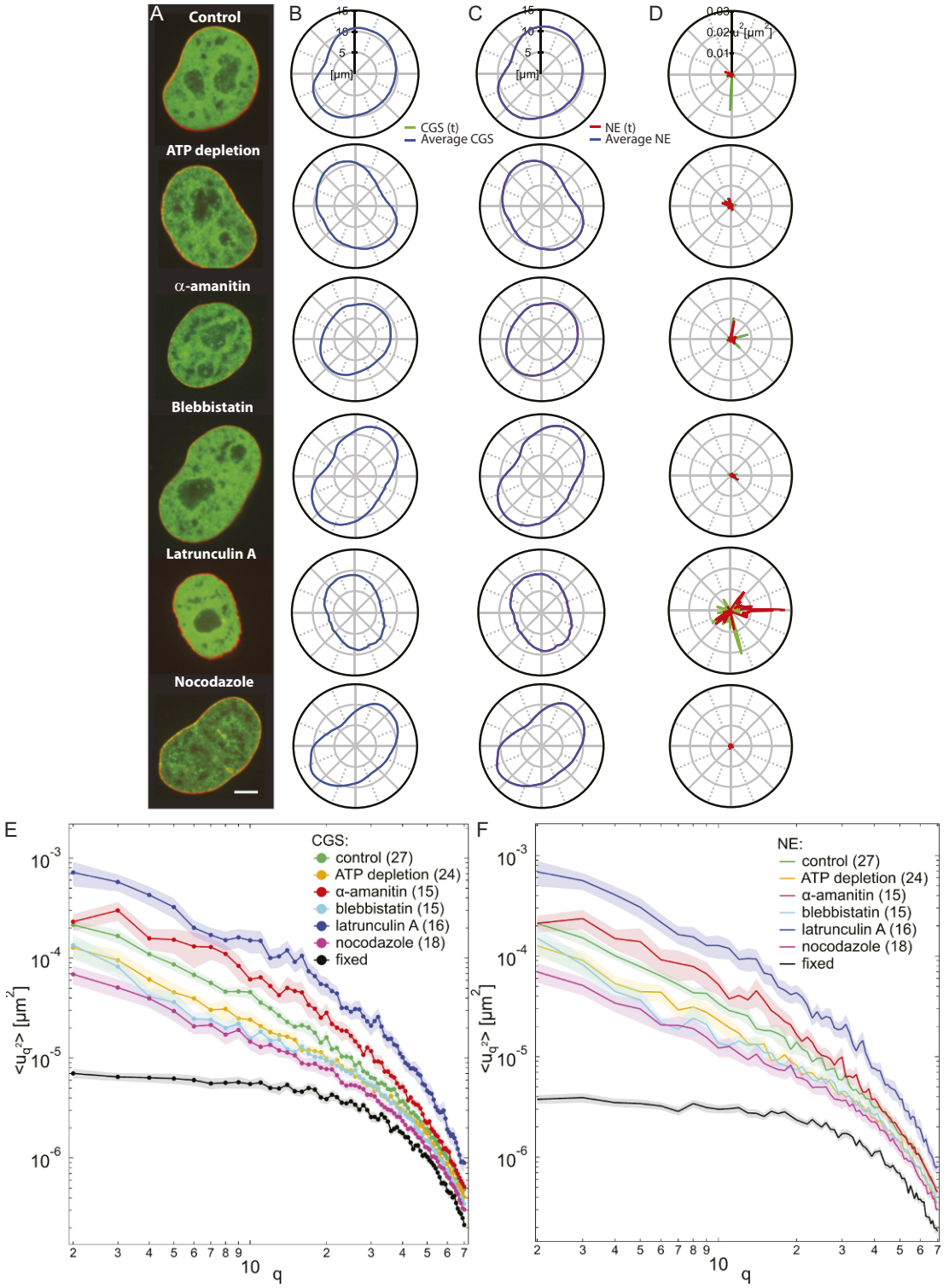

Fig. S6. Simultaneous measurements of shape fluctuations of CGS and NE upon biochemical perturbations. (*A*) Micrographs of cell nuclei simultaneously expressing H2B-mCherry (green) and LMNA-GFP (red) depicting nuclear phenotypes under the following conditions: control, after ATP depletion, and upon addition of α-amanitin, blebbistatin, latrunculin A, and nocodazole. (*B*) Average contour of CGS and instantaneous contour of CGS (H2B-GFP) at one time point for each perturbation. (*C*) Average contour of NE and instantaneous contour of NE (LMNA-GFP) at one time point for each perturbation. (*D*) Fluctuations u^2 of CGS (green) and NE (red) calculated for each condition at one time point; u^2 is strongly reduced upon ATP depletion as well as blebbistatin and nocodazole treatment, and u^2 increases upon addition of latrunculin A. (*E*) The $\langle u_q^2 \rangle$ for CGS plotted with error bars (SE). (*F*) The $\langle u_q^2 \rangle$ for NE plotted with error bars (SE).

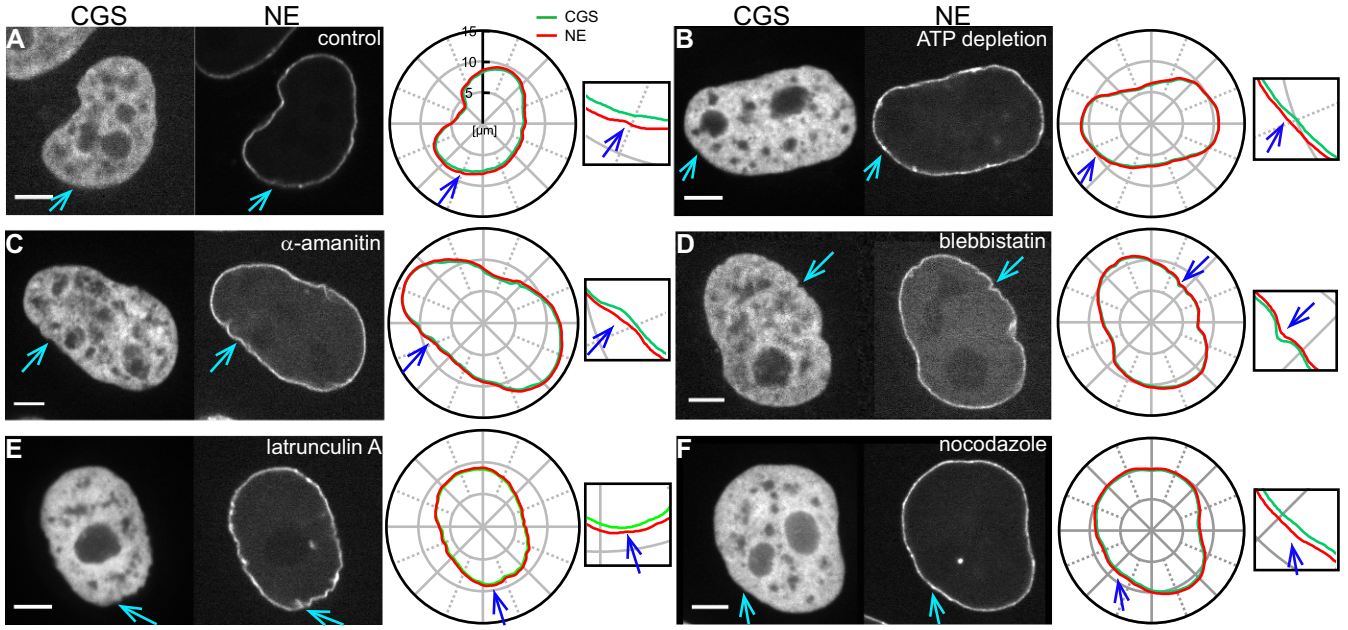

Fig. S7. Example of separation sites exhibited upon different biochemical perturbations. Specifically, micrographs and instantaneous contours for CGS and NE are shown for (*A*) control, (*B*) after ATP depletion, and upon treatment with (*C*) α-amanitin, (*D*) blebbistatin, (*E*) latrunculin A, and (*F*) nocodazole. The separation sites are highlighted by blue arrows in the CGS and NE images and contours. (Scale bar, 5 μm.)

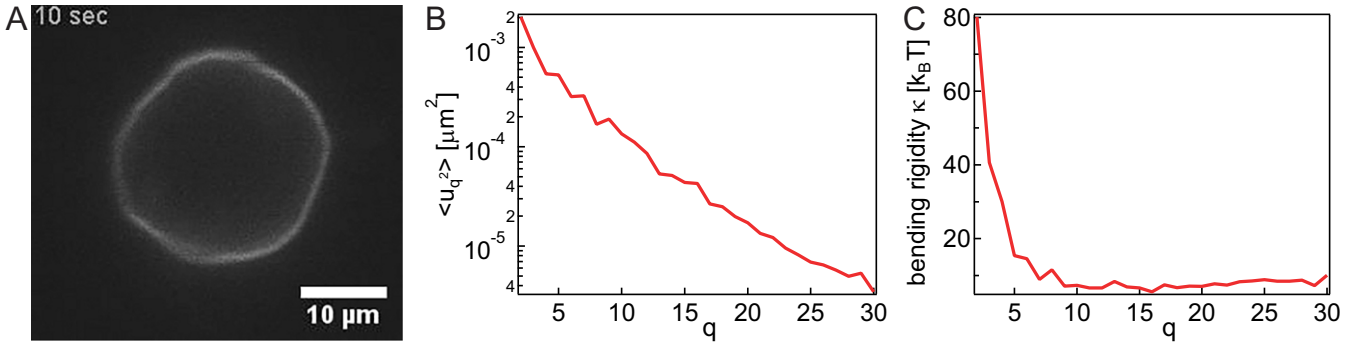

Fig. S8. Control measurement of the contour fluctuations. (*A*) Image of the vesicle from ref. 41, which we used to test the correctness of our contour detection and fluctuation calculation algorithms (movie can be found in ref. 41). Adapted with permission from Loftus et al., Langmuir 29: 14588–14594, 2013. Copyright 2013 American Chemical Society. (*B*) Wavenumber-dependent fluctuations $\langle u_q(t)^2 \rangle$, which we measured for the vesicle from *A*. (*C*) Bending rigidity κ calculated for the vesicle from *A*.

Table S1. Summary of fluctuation characteristics upon biochemical perturbations

Condition	$\langle u_q^2 \rangle$	r_f	k_f	$\tau_{f,1}$	$\tau_{f,2}$	$r_{s,tot}$*	$r_{s,f}$†	k_s	$\tau_{s,1}$	$\tau_{s,2,cgs}$	$\tau_{s,2,ne}$
Control	$\langle u_{q,control}^2 \rangle$	0.66 ± 0.04	0.22 ± 0.04	<1 s	~5 s	0.18 ± 0.05	0.28 ± 0.08	0.07 ± 0.02	<1 s	—	~5 s
ATP depletion	Decrease	0.53 ± 0.06	0.23 ± 0.04	<1 s	~5 s	0.16 ± 0.05	0.30 ± 0.10	0.06 ± 0.01	<1 s	—	—
α-Amanitin	Increase	0.72 ± 0.06	0.25 ± 0.06	<1 s	~5 s	0.15 ± 0.03	0.21 ± 0.05	0.09 ± 0.04	<1 s	~6 s	~6 s
Blebbistatin	Decrease	0.61 ± 0.05	0.21 ± 0.01	<1 s	~5 s	0.20 ± 0.07	0.33 ± 0.11	0.08 ± 0.02	<1 s	~5 s	—
Latrunculin A	Increase	0.92 ± 0.04	0.41 ± 0.06	<1 s	~6 s	0.39 ± 0.06	0.43 ± 0.07	0.09 ± 0.03	<1 s	~5 s	—
Nocodazole	Decrease	0.38 ± 0.07	0.17 ± 0.04	<1 s	~5 s	0.13 ± 0.07	0.33 ± 0.19	0.08 ± 0.02	<1 s	~5 s	—

*Ratio of the number of separation sites to the length of contour.
†Ratio of the number of separation sites to the number of fluctuating sites.